Research Article Vol. 30, No. 8 / 11 Apr 2022 / Optics Express 12695
Optics EXPRESS

Varifocal diffractive lenses for multi-depth microscope imaging

FRANCESCO REDA,[1] MARCELLA SALVATORE,[1,2] FABIO BORBONE,[3,4] PASQUALINO MADDALENA,[1,2,4] ANTONIO AMBROSIO,[4,*] AND STEFANO LUIGI OSCURATO[1,2,4]

[1]*Department of Physics "E. Pancini", University of Naples "Federico II", Complesso Universitario di Monte Sant'Angelo, Via Cintia, 80126 Naples, Italy*
[2]*Centro Servizi Metrologici e tecnologici Avanzati (CeSMA), University of Naples "Federico II", Complesso Universitario di Monte Sant'Angelo, Via Cintia 21, 80126 Naples, Italy*
[3]*Department of Chemical Sciences, University of Naples "Federico II", Complesso Universitario di Monte Sant'Angelo, Via Cintia, 80126 Naples, Italy*
[4]*CNST@POLIMI—Fondazione Istituto Italiano di Tecnologia, Via Pascoli 70, 20133 Milan, Italy*
[*]*antonio.ambrosio@iit.it*

Abstract: Flat optical elements enable the realization of ultra-thin devices able to either reproduce or overcome the functionalities of standard bulky components. The fabrication of these elements involves the structuration of material surfaces on the light wavelength scale, whose geometry has to be carefully designed to achieve the desired optical functionality. In addition to the limits imposed by lithographic design-performance compromises, their optical behavior cannot be accurately tuned afterward, making them difficult to integrate in dynamic optical systems. Here we show the realization of fully reconfigurable flat varifocal diffractive lens, which can be in-place realized, erased and reshaped directly on the surface of an azopolymer film by an all-optical holographic process. Integrating the lens in the same optical system used as standard refractive microscope, results in a hybrid microscope capable of multi-depth object imaging. Our approach demonstrates that reshapable flat optics can be a valid choice to integrate, or even substitute, modern optical systems for advanced functionalities.

1. Introduction

Conventional lenses allow light focusing and imaging formation by exploiting light refraction at spherical surfaces of a bulky component made of a dielectric material (e.g. glass) [1,2]. The optical properties of the medium and the surface macroscopic geometrical parameters, as the radius of curvature and the diameter, determine its functionality by defining the focal length and the numerical aperture. The miniaturization trend demanded by emerging technologies for smartphones, wearables, automotive and virtual reality, is not fully compatible with size and weight requirements of bulky lenses, strongly pushing, instead, the research toward flat and lightweight optical devices able to perform as their conventional counterpart [3].

Flat optical components realize the modulation of the incident light wavefront with thicknesses comparable or even smaller than the light wavelength [4–6]. The optical functionality of these devices is designed by accurately engineering the geometries of light modulating surfaces at micro and nanoscales [7]. Flat optical components acting as beam deflectors, diffraction gratings, lenses and holograms, have been demonstrated over years [8]. Using the laws of light diffraction, flat lenses are traditionally designed as circular apertures in opaque screens or as topographic reliefs with radial symmetry on a dielectric material. Light modulation from these diffractive elements is the result of the coherent superposition of infinite wavelets, emerging from each infinitesimal element constituting the structured surface [7–10]. In addition to diffractive devices, recent developments in the new metasurfaces technology led to the explosion of metalenses, in

#455520 https://doi.org/10.1364/OE.455520
Journal © 2022 Received 3 Feb 2022; revised 11 Mar 2022; accepted 14 Mar 2022; published 31 Mar 2022

Optics EXPRESS

which incident light is modulated, in a subwavelength regime, according to the geometry and the orientation of accurately designed resonant subwavelength scatterers [11].

In both cases, flat lenses bring many advantages in terms of weight saving and reduced dimensions in respect to the standard bulky lenses, constituting valid alternatives to refractive optics in demanding situations, e.g. space exploration [12,13] or depth sensing [14,15]. As further benefits, flat lenses can integrate more functionalities than their refractive counterparts [8] when used alone or when combined with other refractive optics to realize hybrid systems [16–19]. For example, diffractive lenses able to focus light beyond the diffraction limit by exploiting light super-oscillations [20,21], capable of broadband achromatic imaging [22,23], or designed for X-rays focusing or imaging [24,25] have been demonstrated, while new metalenses-based devices with even more advanced functionalities and performances are continuously reported [26–29].

Surface design of these compact devices was widely investigated over years [30,31] in order to optimize their functionality taking also into account the limits imposed by manufacturing techniques. The fabrication process is indeed demanding for devices with high performances and is typically accomplished through complex multistep and multilevel lithographic techniques, whose accuracy strongly affects the ultimate operation performances of the device [32–34]. Furthermore, metalenses require also challenging design and optimization processes that, together with expensive fabrication techniques needed, make their large-scale production more burdensome in respect to diffractive devices [35]. However, several conventional lens applications, as light focusing and imaging, do not often require the highest performances offered by metalenses, and even diffractive lenses, when properly designed and fabricated, can provide remarkable optical quality, while maintaining the advantage of a simpler and cheaper design and manufacture [36,37].

After the fabrication process of standard lithography, the crucial parameters for lens operation, like the focal length and the focusing efficiency, are essentially frozen. This limits the possibility to use them as dynamically tunable devices only in sophisticated systems [38–45] and with limited tunability ranges [41,46,47], becoming not suitable where dynamic optical devices are required [48,49]. Tunable diffractive lenses can be, for example, realized using liquid crystals (LC) devices with many limitations in terms of layer thickness and tunability range and also additional challenges related to their strong polarization dependence [50].

We recently moved forward in this direction by developing a reversible lithographic technique for creating diffractive surfaces on azopolymer thin films [51,52]. We demonstrated the realization of fully reconfigurable phase-modulating diffractive surfaces with engineered diffraction behavior such as reconfigurable flat lenses, extending the design proposed by Gabor for the realization of amplitude zone plates [53–55]. Similar to a familiar diffraction grating, these lenses produce multiple diffraction orders, each focused at different positions of the optical axis. By acting as intrinsic multifocal lenses, both positive and negative, then, these devices could be useful in several applications, as the realization of a compact radial shearing interferometer [56].

In this work we further investigated focusing and imaging properties of lenses realized as cosinusoidal phase zone plates, showing that the multifocal behavior can be also applied in the design of advanced hybrid imaging systems, based on both refractive and diffractive optics. In particular, we show here the realization of a hybrid microscope with controllable magnification, field of view and working distance, obtained using a diffractive reconfigurable lens acting as a Barlow lens. This lens is directly realized on the surface of a photo-responsive azobenzene-containing polymer, which can be completely re-morphed in-place to achieve different parameters, as focal length and numerical aperture, by an all-optical reversible lithographic process. Our approach proves the benefits of well-engineered flat optics that in the future can integrate or even replace standard optics, leading to compact, lightweight, low cost and high performances optical systems.

Optics EXPRESS

2. Phase-only cosinusoidal zone plate lenses

The cosinusoidal Phase Zone Plate (c-PZP) is the counterpart to the amplitude Gabor zone plate [53,55], in which the alternating absorbing and transmitting circular zones are replaced with transparent phase modulating zones, each imposing a position dependent phase delay on the incoming wavefront. In the same way that a diffraction grating separates an incoming plane wave into a sum of emerging plane waves with different wavevectors, a c-PZP acts as a phase grating with circular symmetry and radially variable groove spacing, splitting an incident wave into a sum of spherical emerging waves, each converging at distances f_m from the lens, where the integer number m defines the focal diffraction order.

For an incoming monochromatic plane wave at wavelength λ, travelling in positive z direction, the transversal (in x-y plane) phase modulation produced by the cosinusoidal zone plate is [30]:

$$\varphi(x, y) = \varphi(r) = \frac{\beta}{2}(1 + \cos(\alpha r^2)). \tag{1}$$

Here, the parameter β is the maximum phase modulation depth imposed on the incident wavefront, the parameter α is related to lens geometry and determines the first order focal distance $f = f_{+1}$, and $r = (x^2 + y^2)^{1/2}$ is the radial coordinate in c-PZP plane.

This phase profile can be realized through a structured dielectric surface with periodicity-varying grooves, which encodes the required phase modulation pattern in local optical path differences for the incident wave, travelling in surface medium with refractive index $n = n(\lambda)$ and local thickness $h(x,y)$. If the medium surrounding the structured dielectric is air, as schematized in Fig. 1(a), the maximum phase modulation depth β is proportional to the relief height h, according to:

$$\beta = \frac{2\pi}{\lambda}(n - 1)h. \tag{2}$$

The explicit relation between the parameter α and the first order focal distance f of the c-PZP is obtained by requiring constructive interference at $z = f$ of the wavelets emerging from the topographic maxima (or minima) of the surface:

$$\alpha = \frac{2\pi}{\lambda^2 - 2\lambda f}. \tag{3}$$

Diffraction properties of a c-PZP are strongly related both to the relief height and to their lateral geometry. This becomes clear if the phase zone plate is represented through a radial complex transmittance function $t(r)$ modulating, in the scalar approximation of wave optics, the wavefront of an incident optical field U_{in} propagating through the device. In this situation, the optical field U_{out} immediately after the phase mask is given simply by $U_{\text{in}} \cdot t(r)$. In the case of a c-PZP, $t(r)$ can be written as:

$$t(r) = \exp[i\varphi(r)] = \exp\left[i\frac{\beta}{2}(1 + \cos(\alpha r^2))\right]. \tag{4}$$

This complex transmittance function can be expanded in the base of radial harmonics using the Jacobi expansion [57], resulting in [30]:

$$t(r) = t_0 \sum_{m=-\infty}^{+\infty} i^m J_m\left(\frac{\beta}{2}\right)\exp(im\alpha r^2), \tag{5}$$

where t_0 is a constant phase term, i^2=-1, J_m is a first kind Bessel function of the m^{th} order, and β and α are the surface structural parameters given in Eq. (2) and (3), respectively. Assuming that the light wavelength is negligible compared to the focal length ($\lambda \ll f$), λ^2 can be neglected in

Optics EXPRESS

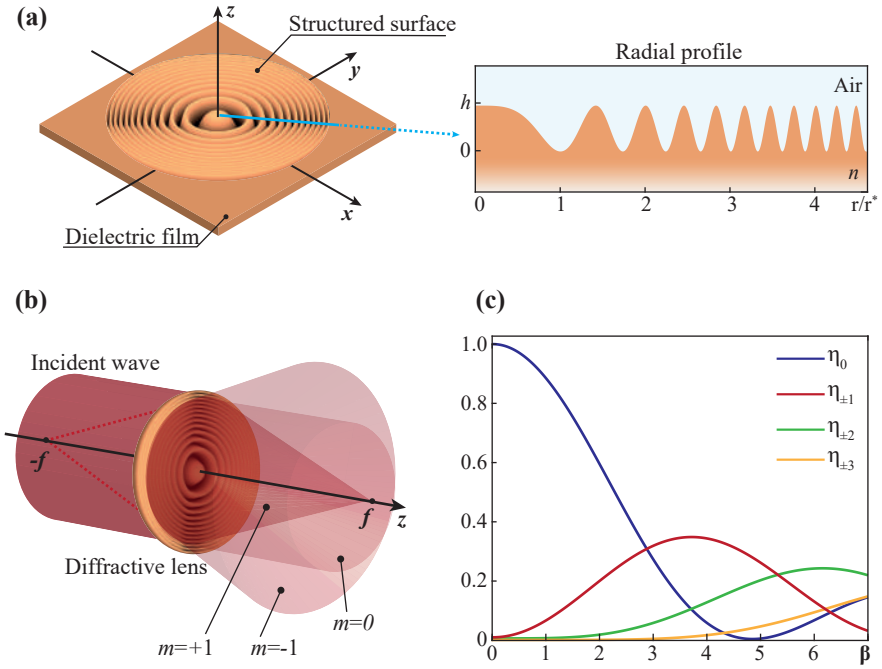

Fig. 1. Design and functionality of a phase-only cosinusoidal zone plate (c-PZP) lens: (a) Schematic of a Gabor zone plate realized on the surface of a dielectric film. Inset shows the radial profile of the cosinusoidal Gabor zone plate, obtained by renormalizing the radial coordinate with respect to the distance of the first minima in the phase mask: $r^* = (\pi/\alpha)^{1/2}$. (b) Schematic of the multiple diffraction foci produced by a c-PZP lens. (c) Diffraction efficiency of first seven diffraction orders plotted with respect the maximum phase mask modulation depth β, directly related to the surface relief amplitude h for a given material of refractive index n.

Eq. (3), so that the expansion in Eq. (5) demonstrates that a c-PZP has a transmission function of a multifocal lens. A plane wave incident on the device emerges as a sum of spherical waves with focals that are fractions of the first order focal length $f_m = f/m$. As schematized in Fig. 1(b), each of the emerging waves represents a specific diffraction order: spherical divergent ($m < 0$), spherical convergent ($m > 0$) and a plane wave ($m = 0$), that corresponds to the unmodulated component. An ideal c-PZP introduces no energy loss, and $|t(r)|^2 = 1$. In this case, the square modulus of each term of the sum in Eq. (5) represents the fraction of energy carried by each emerging spherical wave, allowing the definition of the focusing efficiency for a given order m as:

$$\eta_m = \left| J_m\left(\frac{\beta}{2}\right)\right|^2. \tag{6}$$

This parameter, defined as the intensity of light in each focus f_m, normalized with respect to the incident light intensity, is directly related to the modulation depth β, which then determines, through the relief amplitude h, the redistribution of the incident light power in the emerging diffraction orders. In Fig. 1(c), the efficiency $\eta_m(\beta)$ for the first seven diffraction orders produced by a c-PZP is plotted. Maximum focusing efficiency of ≈ 34% is obtained in the first order (m=±1) for the value $\beta^* \approx 3.68$. For a dielectric surface with $n = 1.7$ (like the one used in this work) this condition is achieved, for monochromatic light at λ=633 nm, at $h \approx 530$ nm. A diffractive c-PZP lens of optimized efficiency can be then realized with thickness smaller than

Optics EXPRESS

the incident light wavelength. It is worth noting that the diffraction efficiency as defined by Eq. (6) does not depend on the sign of m so, if the efficiency of one of the real focal diffraction orders ($m > 0$) is suitably optimized, the same amount of incident light is diffracted also in the corresponding virtual focal order ($m < 0$).

A c-PZP can be also used for imaging [51]. In geometric optics the imaging process of a lens is a form of information transfer between the object plane and an imaging plane. The axial position where the image is formed (imaging plane) is determined by both the axial object position (object plane) and by the focal length of the lens, according to the conjugate planes law [1]. These relations remain valid also for the description of the image formation from a multifocal c-PZP, which simply requires a generalization of the Newton equation for thin lenses [7], in order to take into account for the simultaneous presence of multiple focal lengths, each for every diffraction order m:

$$\left(p - \frac{f}{m}\right)\left(q - \frac{f}{m}\right) = \left(\frac{f}{m}\right)^2. \tag{7}$$

As usual, in Eq. (7), p is the distance between the object and the lens, q is the position of the image plane relative to the plane of the lens, and f is the designed focal distance for the first diffraction order. This relation can be useful to design versatile optical imaging systems working as multifocal diverging or converging lenses. For example, a c-PZP can be used with the same efficiency simultaneously in microscope and telescope configurations. In the first case, the diffractive lens must act as a diverging lens, like the standard objective lens of a compound microscope, while the second configuration is realized with a simple converging lens, able to image objects placed at large distances [51]. Considering a fixed focal length $|f_m|$, in a c-PZP, the two operating regimes correspond to two sets of foci with the same value of m (for example, m=−1 and m=+1, for the microscope and the telescope configuration, respectively), and same diffraction efficiency.

Moreover, if the geometry of the c-PZP can be modified in real time to affect its efficiency, or its focal length f, as happens for diffractive surfaces realized as light-induced surface reliefs on azopolymer films [51], even more functionalities can be realized form Eq. (7), as tunable telescope zoom imaging systems [51] or a multi-depth microscope able to focus at objects placed at different positions.

3. Realization of azopolymer c-PZPs

For the realization of reconfigurable c-PZP, we have used an amorphous azobenzene-containing polymer film (azopolymer), whose surface can be structured through a direct single-step optical lithographic process. The light-induced structuration of these materials originates from a macroscopic material displacement, triggered by cyclic light-fuelled photo-isomerization of the azobenzene units included in the material via different chemical interactions [58–63]. The resulting surface reliefs on the azopolymer free surface are strongly dependent on both the intensity distribution and polarization of the incident light. In the case of circularly polarized light in low intensity regimes [51,64], the relief geometry is proportional to the Laplacian of the intensity pattern [65] and the average surface relief height increases linearly with the total exposure time [51,52].

Light structuration on the film surface can be easily achieved using interference [52,66–69] but in this work we used a Computer-Generated Hologram (CGH) setup based on a Spatial Light Modulator (SLM), which allows to project an arbitrary grayscale spatially structured intensity distribution of light on the surface of the azopolymer film, directly transferring the desired relief geometry on the material surface [64]. We realized the optical setup with a microscope configuration allowing the in-place fabrication [51], characterization and operation of the azopolymer diffractive lenses.

Optics EXPRESS

The scheme of the optical system is presented in Fig. 2(a). An expanded TEM_{00} laser beam (Cobolt Calypso, at wavelength 491 nm) is phase modulated by a computer-controlled reflective phase-only Spatial Light Modulator (Holoeye, Pluto). The modulated beam is propagated through a 4*f* lenses system with the input plane located in the SLM plane. An iris allows spatial filtering of the unwanted components emerging from the SLM. The output plane coincides with the back focal plane of an infinity-corrected long-working distance 50X objective (Mitutoyo), with numerical aperture NA = 0.55 and 13 mm working distance. The writing beam is circular polarized by means of a quarter wave plate (QWP) and its measured intensity, in the sample plane, is approximately 14.0 W/cm^2. This configuration allows the reconstruction of arbitrary structured intensity patterns in the focal plane of the objective, where the azopolymer film is placed. The phase profile (*kinoform*) to be imposed in the SLM plane to reconstruct the desired holographic distribution is defined by an iterative Fourier transform algorithm (Mixed Region Amplitude Freedom (MRAF) algorithm [70]), implemented in MATLAB. The calculation process is initialized providing a target 8-bit grayscale image, shown in Fig. 2(b), representing the desired intensity pattern to be finally reconstructed in the azopolymer plane. Additional details about holographic system and the MRAF algorithm used here can be found in our previous work [51].

The optical image of the intensity hologram, reconstructed in the sample plane, to realize a c-PZP with focal length of $f = 0.6$ mm at λ=633 nm, is shown in Fig. 2(c). This image is acquired through a tube lens (TL) and a CCD camera, that collect the light retroreflected by the sample surface by means of a 70:30 (T:R) beam splitter, Fig. 2(a). The holographic image is the result of an averaging process: many independent calculated kinoforms are buffered to the SLM with a repetition rate of 20 Hz, in order to reduce speckle noise and improve contrast and resolution in the average holographic intensity pattern [64,71].

In the azopolymer structuration processes, an additional diode laser beam at 405 nm illuminates the sample film from the substrate (a standard glass microscope coverslip) side. This beam has circular polarization and different intensity levels depending on its intended role. For low intensity regimes (0.5 W/cm^2) the beam enhances the surface structuring process acting as a writing *assisting* beam. At higher intensity (0.9 W/cm^2), its absorption causes the erasure of previously inscribed surface structures, acting as an *erasing* beam [51,72].

The optical system in Fig. 2(a) can also be used as a brightfield microscope, integrating the holographic setup with a collimated white LED source that simultaneously illuminates the sample, to reconstruct an image of the surface in the camera plane during the lithographic exposure process. The image is reconstructed with a magnification of 50X, according to tube lens and objective focal lengths. Figure 2(d) shows the optical image of the azopolymer surface after 45s of irradiation with the holographic pattern sequence. This exposure time, according to our previous calibration [51], optimize the average relief height ($\approx$ 530 nm), ensuring maximum diffraction efficiency of the lens in the first diffraction order for our material, whose refractive index is equal to 1.7 at the selected working wavelength (λ=633 nm). A detailed morphological characterization of the polymer surface after irradiation by means of Atomic Force Microscopy (AFM) is provided in our previous work [51].

Optics EXPRESS

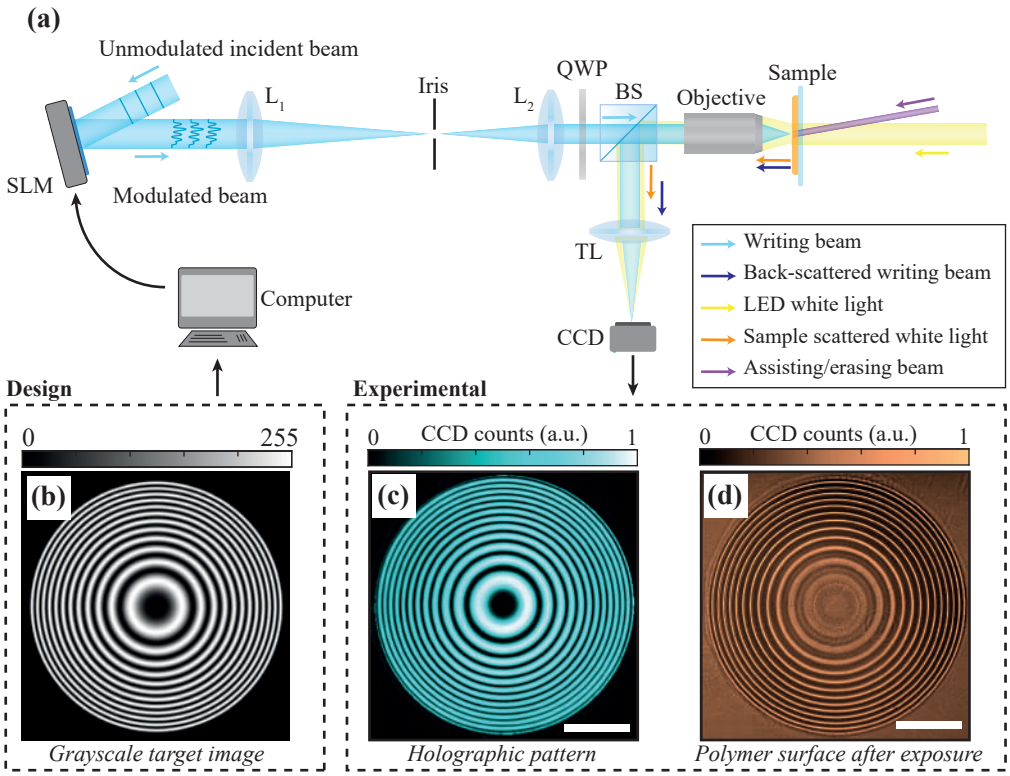

Fig. 2. Experimental realization of a cosinusoidal Gabor lens using holographic inscription on azopolymer film: (a) Representation of the holographic lithography setup: the SLM realizes a 4*f* configuration with a biconvex lens (L_1) with focal length equal to 300 mm, a biconvex lens (L_2) with focal length equal to 175 mm and the objective. A beam splitter (BS) allows the collection of retroreflected light. Light is focused with a tube lens (TL), with 200 mm focal length, on a "DCC3240M Thorlabs" camera (CCD Camera). Colored arrows indicate the direction of the writing beam, the LED beam, and the scattered components from the surface. (b) Gray scale image representing the target image used for generating the holographic pattern through the iterative algorithm. (c) Reconstructed hologram in the sample plane for the realization of a cosinusoidal Gabor zone plate. (d) Optical image of the azopolymer free surface, after 45 seconds of irradiation with both the holographic and the assisting beam, obtained with the brightfield microscopy. Scale bar in panels (c-d) correspond to a physical dimension of 50 µm. CCD counts were remapped in the interval [0 1].

4. Focusing properties of azopolymer c-PZPs

In order to characterize the focusing properties of the realized c-PZP, the emerging light diffraction pattern has been first simulated for an incident plane wave with wavelength λ=633 nm, modulated by the diffractive lens according to the transmission function shown in Eq. (4). In the simulation, material refractive index $n = 1.70$ and relief amplitude $h = 530$ nm, have been considered [51]. In the simulation, the diffractive surface is described as a circular structured area with radius R = 96.4 µm, which corresponds to the radius of the field of view of our holographic writing system. Assuming the modulated surface at $z = 0$, the optical field propagated in any plane at the axial position z is evaluated by solving Helmholtz equation, using the Rayleigh-Sommerfeld diffraction integral in Fresnel approximation [73]. For the simulation, Fresnel integral has been

Optics EXPRESS

numerically implemented in MATLAB using the convolution theorem with the transfer function of the Fresnel propagator [74]. Simulation results are provided in Fig. 3(a) where the axial Point Spread Function (PSF) for a c-PZP with $f = 0.6$ mm is plotted.

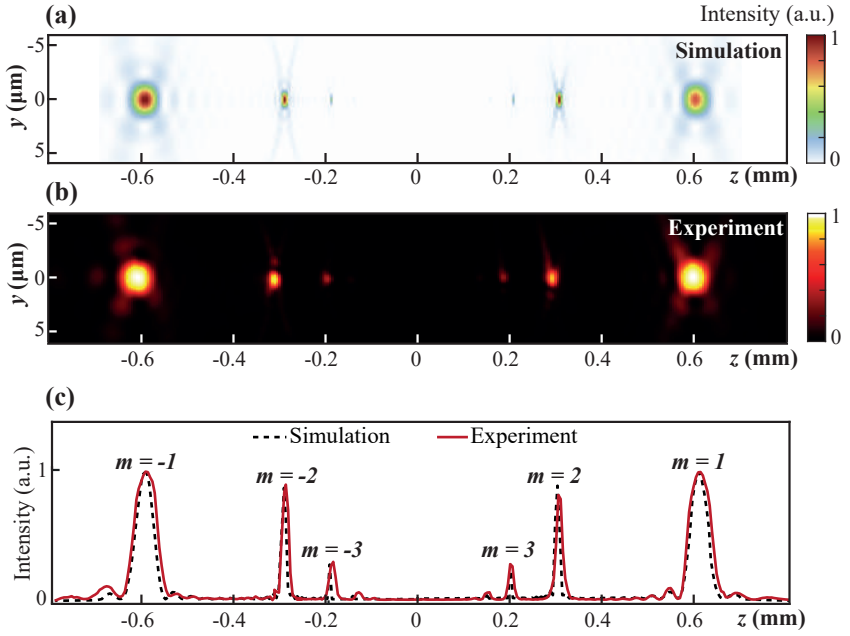

Fig. 3. Focusing properties of realized c-PZP: (a) Simulation of the y-z point spread function obtained evaluating intensity distribution of the optical field. Simulation is performed in the z range (−0.80 mm to 0.80 mm) and in y range (−6.0 μm to 6.0 μm). (b) Experimental PSF reconstructed by collecting the diffracted field from a He-Ne laser beam. CCD counts were remapped in the interval [0 1]. (c) Normalized experimental axial intensity profile of the PSF compared with the axial profile provided by the simulation.

Experimental measurement of the PSF has been performed using a collimated circularly polarized He-Ne laser beam (λ=633 nm), orthogonally incident on the diffractive lens from the substrate side. Light diffracted by the lens is collected though the same microscope imaging system used for brightfield surface observation. The images of the transmitted He-Ne intensity pattern, at different positions, have been obtained by axially translating the c-PZP with a manual micro-positioner. For each sample position, determined with steps of 0.005 mm, an image of the field intensity profile is acquired using the CCD in the focal plane of the tube lens. The images are then stacked together to reconstruct the experimental PSF (Fig. 3(b)). The experimental axial intensity profile, shown in Fig. 3(c) together with the analogous simulated profile, confirms the predictions of the scalar diffraction theory for a c-PZP. The c-PZP acts as a multifocal lens with first diffraction order focal spots at $z = f_{\pm 1} = \pm 0.6$ mm. Both real and virtual foci have the same relative axial intensity, as predicted by Eq. (6).

Focal spot characterization has been performed acquiring the focal intensity distribution for real and virtual foci (m=±1) and their relative transversal profiles, shown in Fig. 4(a-c), respectively. In order to quantitatively describe quality of the focus, we have used the Strehl ratio as figure of merit. The Strehl ratio (SR) is defined as the ratio of the peak intensity $I_{measured}(0)$ in the focal plane with respect to the intensity of an ideal Airy disk (AD), normalized in order to have the

Optics EXPRESS

same area under the curve with respect to the experimental profile [75]:

$$SR = \frac{I_{measured}(0)}{I_{ideal}(0)} = I_{measured}(0)\frac{\lambda^2 f^2}{P_0 \pi R^2}, \tag{8}$$

where P_0 is the normalization factor for the ideal peak intensity $I_{ideal}(0)$ at the center of the diffraction pattern produced at distance $z = f$ by a circular aperture with radius R [76]. For an ideal lens with a diffraction limited behavior and focal intensity distribution of an Airy disk, the Strehl ratio is 1. In real cases, even small aberrations affecting lens functionality cause a significant drop of SR toward smaller values. A SR greater than 0.8 typically denotes a diffraction limited performance for a real lens [75]. In our case a SR = 0.79 has been obtained for both real and virtual focal spots, comparable with values reported for high quality metalenses [26,77].

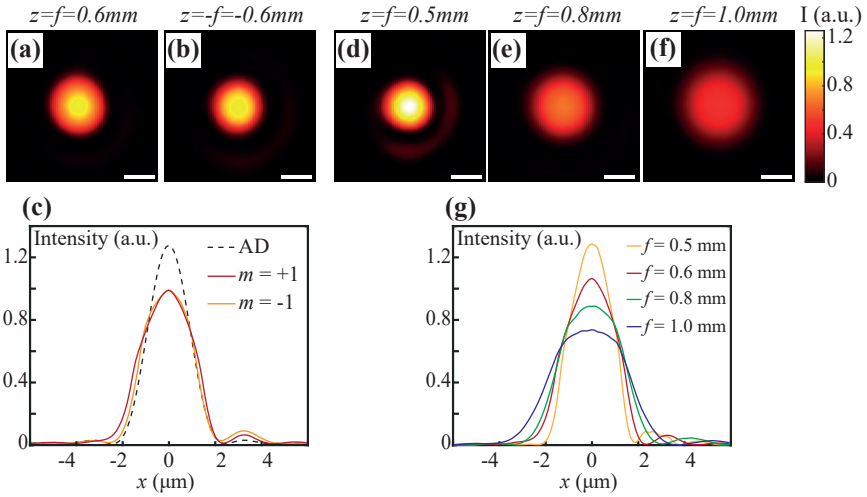

Fig. 4. Characterization of the focal spot quality: (a,b) Light intensity distribution of the first order focal spot of a c-PZP with nominal focal length $f = 0.6$ mm. Images are acquired at $z = f$ and $z = -f$, respectively. (c) Plot of the x-profiles of both real (m=+1) and virtual (m=−1) first order focal spot of the lens with $f = 0.6$ mm and simulated profile of an ideal Airy Disk (AD) used for the evaluation of the Strehl ratio. (d,e,f) Light intensity distribution of the real first order focal spot of c-PZPs with nominal focal length equal to 0.5, 0.8 and 1.0 mm. Images were acquired with the same exposure time fixed for the lens with 0.6 mm focal length. Scale bar in panels (a,b,d,e,f) correspond to a physical dimension of 2 μm. (g) Plot of the experimental focal spot x-profiles obtained at different focal lengths.

The same analysis has been repeated also for c-PZP designed with different focal lengths, obtained by properly reshaping the diffractive lens through azopolymer erasure and rewriting processes. Figure 4(d-f) shows the first order focal intensity distribution for three diffractive lenses with f equal to 0.5 mm, 0.8 mm and 1.0 mm respectively. These lenses are obtained by exposing the same free azopolymer surface area to a proper holographic pattern (after erasure step) with fixed holographic irradiation parameters (intensity and irradiation time). Strehl ratio of 0.78, 0.83 and 0.81 have been respectively obtained for experimental intensity profiles, reported in Fig. 4(g). Since the diameter of the c-PZP are fixed by the field of view of the optical setup, the Numerical Aperture (NA) of the lenses is inversely proportional to the focal length. Accordingly, the Full Width at Half Maximum (FWHM) of the focal spots increases with the focal length. The total optical power in the focal spot, measured by integrating the intensity distribution shown in Fig. 4(a,d,e,f) over a circular area with diameter three times of the FWHM, is conserved within 91% by changing the focal length. This ensures that the erasing and rewriting process of a new

Optics EXPRESS

c-PZP with the same writing parameters will preserve the overall quality of the lens focal spot in terms of both efficiency and aberrations. In order to characterize the noise contribution produced by the defocused diffraction orders in the focal plane, we measured the Signal to Noise Ratio (SNR) from the acquired focal spot profiles reported in Fig. 4(g) defined as the ratio between the intensity profile maxima (I_{max}) and minima (I_{min}). The analysis provided a minimum SNR of ~22 dB, that correspond also to a minimum spot visibility, defined as $(I_{max} - I_{min})/(I_{max} + I_{min})$, of 0.99, confirming small contribution in the focal plane from other out of focus diffraction orders.

It is worth mentioning that our current setup allows the realization of c-PZPs with focal lengths in the range from 0.3 to 1.2 mm, with limits dictated only by the resolution of the holographic system and by objective field of view. Using different combinations of optics and SLM for the holographic projection, we could easily expand this range. However, in the operating focal length range, our c-PZPs can be fully in-place reshaped with no quality loss, allowing the realization of dynamical light focusing systems.

5. Hybrid Barlow lens configuration for multi-depth microscope imaging

An ideal imaging optical system, such as an optical microscope, reconstructs in a specific plane of the optical axis, the image, eventually inverted and magnified, of objects lying in a range of planes determined by the depth of field of the system. Typically, microscope objectives, as the one composing our setup in Fig. 2(a), are designed with very short depth of field in order to increase their lateral and axial resolution. For such systems, sharp imaging is limited only to objects placed at a fixed distance from the front lens of the objective, that is defined as the working distance.

The field of view of a microscope can be enlarged properly translating, replacing or integrating the optical elements composing the system. An example is represented by Barlow lenses. A Barlow lens is a diverging lens that increase the focal length of an imaging system. As a result, also its field of view is accordingly increased [78]. When used in microscopy, the working distance of a system equipped with a Barlow lens is increased and the magnification power of the microscope is reduced.

The working principle of a standard refractive Barlow is schematized in Fig. 5(a): this lens, with focal length f, is placed after the front lens of a converging lens (e.g. an objective). The lens forms a virtual image of an object placed at distance z_O from the plane identified by the working distance (WD), assumed to be at $z = 0$ in our coordinate system. If the position z_L of the Barlow lens is properly chosen according to its focal length, the virtual image from this lens is reconstructed in the imaging plane (at $z = 0$) of the objective and transformed then into a real image by the subsequent optical elements in the microscope.

Due to the presence of virtual foci, diffractive c-PZPs can be directly used as Barlow lenses in refractive/diffractive hybrid imaging systems. When realized on azopolymers, the c-PZPs can even enlarge the range of applications behind the field of extender of classical Barlow lenses, due to the possibility of dynamically changing their focal length. In this work, we implement the c-PZP Barlow imaging configuration directly combining the holographic system and the lithographically produced c-PZPs on azopolymer films, as schematized in Fig. 5(b). As a results, we obtain a hybrid microscope composed of a part of fixed refractive optics and a reconfigurable cosinusoidal zone plate, whose focal length can be tuned on demand through an in-place all-optical reshaping process of the azopolymer surface. This system can provide images of extended objects placed at arbitrary positions of the optical axis by proper tuning both the position and the focal length of the c-PZP.

The object used for our experiments is a microscope calibration target (from Thorlabs) composed by a grid of orthogonal lines, with spacing of 50 μm, printed on a glass substrate. The object is mounted on a manual micro-positioner that allows its translation along the optical axis. A reference image of the object, obtained by placing the grid in the objective focal plane ($z_O = 0$)

Optics EXPRESS

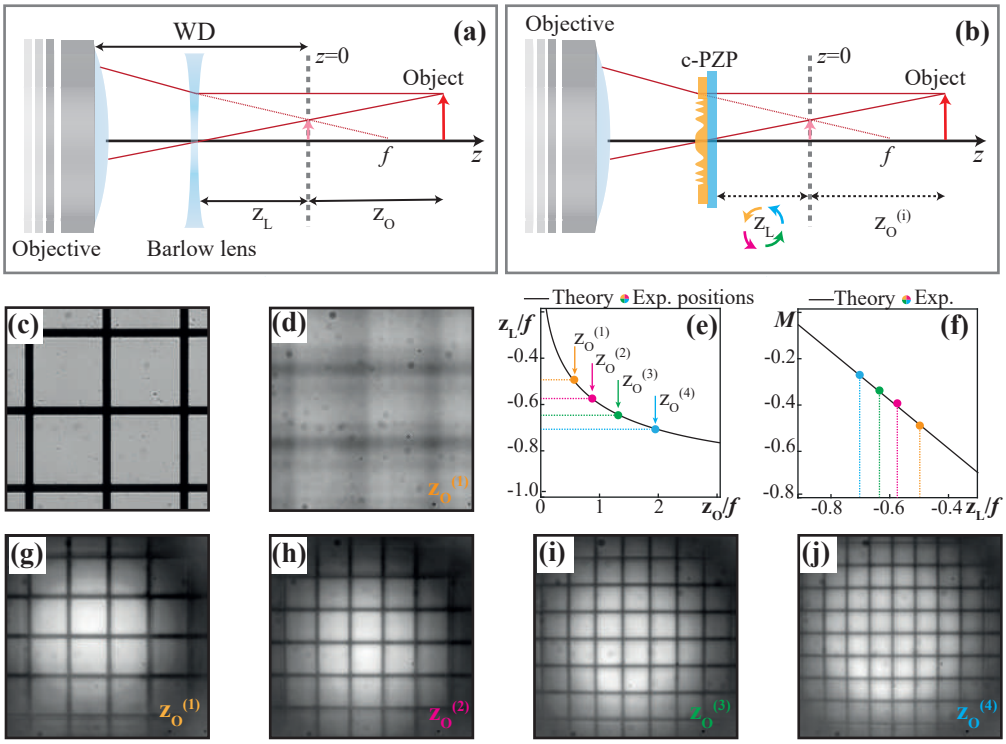

Fig. 5. Barlow lens configuration for multi-depth imaging microscope. (a) Representation of the working principle of a Barlow lens coupled with a microscope objective. (b) Barlow lens can be easily replaced with a c-PZP obtaining the same effect. (c) Optical image of the calibration grid with grid spacing equal to 50 µm. Image is obtained fixing the grid position at $z_O = 0$ before the azopolymer structuration. (d) Optical image of the grid at $z_O = 0.300$ mm. (e) Theoretical and experimental values for the ratio z_L/f of the diffractive lens with respect to the object position z_O/f. (f) Theoretical and experimental values for the magnification with respect z_L/f . (g) Optical image of the grid obtained for $z_O^{(1)} = 0.300$ mm and $z_L^{(1)} = -0.300$ mm. (h) Optical image of the grid obtained for $z_O^{(2)} = 0.500$ mm and $z_L^{(2)} = -0.350$ mm. (i) Optical image of the grid obtained for $z_O^{(3)} = 0.800$ mm and $z_L^{(3)} = -0.400$ mm. (j) Optical image of the grid obtained for $z_O^{(4)} = 1.100$ mm and $z_L^{(4)} = -0.430$ mm. Images in panels (e,f,g-j) were obtained fixing the CCD region of interest in order to highlight magnification effects.

before that the c-PZP is inscribed on the azopolymer film, is shown in Fig. 5(c). This image, is reconstructed collecting scattered light from the object, transmitted through the flat azopolymer film which was already aligned in the microscope light-path.

When the object is moved in a new position (e.g. $z_O^{(1)} = 0.300$ mm) using the micro-positioner (with sensitivity equal to 0.005 mm), the resulting out-of-focus image acquired by the CCD camera appears blurred, Fig. 5(d). To bring back the image in focus, a diffractive lens with $f = 0.6$ mm is holographically inscribed on the azopolymer film, by first translating the azopolymer film in the lithographic plane at $z = 0$ and then re-translating the structured film with the c-PZP in the working position z_L, found from Newton equation (Eq. (7)) imposing that the diffractive lens

Optics EXPRESS

of focal f forms an image of the object at $z = 0$:

$$\frac{z_L}{f} = \frac{1}{2}\left(\frac{z_O}{f} - \sqrt{\frac{z_O^2}{f^2} - \frac{4z_O}{mf}}\right). \tag{9}$$

Only the class of solutions such that z_L is in a finite range is considered, in order to realize a more compact optical system. Despite classical Barlow configuration requires a negative focal length ($m < 0$) placed between the microscope lens and the object ($z_L < 0$), in writing Eq. (9), we explicitly maintained the diffractive lens focal order m still unspecified in order to highlight some of the advantages of building a hybrid imaging configuration based on a c-PZP. From Eq. (9), indeed, for every position of the object z_O, at least two distinct positions z_L of the diffractive lens can realize the imaging condition, each corresponding to an explicit choice of $|m|$ and $sign(m)$. Limiting the discussion to the first order foci ($|m|$=1) of c-PZPs, that have the maximum diffraction efficiency, if m=+1 (converging lens), image formation is possible only if the c-PZP is placed in the same half space of the object ($z_L > 0$), and only if the object lies at distances larger than four times the focal length f of the lens ($z_O > 4f$). This configuration works as a microscope with extended depth of field, able even to image large objects placed very far (at $z_O \gg 0$) from the original imaging plane (telescope configuration), as we demonstrated recently by our azopolymer-based c-PZPs [51]. Conversely, the same c-PZP operates simultaneously as a classical Barlow lens through its negative focal order (m=−1), resulting in a compact ($z_L < 0$) imaging system with extended depth of field.

The solid line plot in Fig. 5(e) shows the correct positions (in units of f) for the azopolymer c-PZP Barlow lens calculated by solving Eq. (9) for different normalized positions z_O/f of the object translating along the optical axis. From the plot, is evident that any position of the object is correctly imaged by the system by tuning the ratio z_L/f of the azo c-PZP in a finite domain.

Newton equation allows also to define the magnification power M of the system by extending the standard equation of linear magnification [1] valid for a thin glass lens to a diffractive multifocal c-PZP:

$$M = m\frac{z_L}{f} - 1, \tag{10}$$

whose solutions, obtained for m=−1, are plotted in Fig. 5(f).

According to the solution of Eq. (9), by positioning in the experiment the azopolymer c-PZP with f = 0.6 mm at z_L=−0.300 mm, the previously blurred object placed at $z_O^{(1)}$ = 0.300 mm appears again in focus in the area of the image identified by the aperture of the diffractive lens, Fig. 5(g). As the hybrid configuration grants a high axial selectivity for image formation, no contributions from other diffraction orders are visible, allowing for the reconstruction of an hight contrast image as result of the achieved efficiency-optimized condition for the azopolymer c-PZP.

Also, the measured magnification is in accordance with theoretical predictions of Eq. (10). To further prove the correct image reconstruction of the hybrid microscope, we sequentially moved the position of the object along the optical axis, before re-gaining an in-focus image by adapting the position of the diffractive c-PZP lens. The tested position pairs ($z_O^{(i)}$, $z_L^{(i)}$) are shown as experimental points in Fig. 5(e), while Fig. 5(f) shows the experimental magnification measurements obtained from the focused images of the grid, Fig. 5(g-j), compared to theoretical prediction.

Regarding the quality of the image produced by the hybrid Barlow system in Fig. 5(g-j), one should consider that, similar to standard diffractive lens, the c-PZP is designed here to focus only beams with normal incidence with respect to the structured surface. This condition is no longer true if the object is placed very close to the lens. As a result, a loss of contrast is observed at the periphery of the images, where the angle of the incidence increases. This aberration effect, known as vignetting, is typically observed in diffractive imaging systems [79], and could be

Optics EXPRESS

eventually reduced by properly designing an optimized radial surface profile for the diffractive lens [80].

The results in Fig. 5(g-j) demonstrate a successful realization of a hybrid microscope that requires only the motion of a thin and lightweight diffractive component to provide in focus images of objects placed at different axial positions. However, together with the physical motion of the diffractive lens, the in-place all-optical reconfiguration of the azopolymer can be used to realize varifocal c-PZP Barlow lenses with advanced functionalities.

An example is the possibility to realize an operating Barlow configuration with a fixed position z_L of the varifocal diffractive lens. According to Eq. (9), the operation of the in focus image of a translating object along the axis can be recovered by substituting the translation of the c-PZP lens (as schematized in Fig. 5(b)) with a shift of the focal length f to tune the ratio z_L/f (Fig. 6(a)). Figure 6(b-d) show the in-focus images of the object placed at different positions $z_O^{(i)}$ obtained by reconfiguring the focal length of a Barlow c-PZP lens at proper values $f^{(i)}$, satisfying Eq. (9) for a fixed position of the lens z_L=−0.300 mm. It should be noted that a similar approach for multi-depth imaging requires a high precision lens fabrication to match the analytically calculated values of the focal length. With our holographic system, this requirement is instead accomplished effortlessly, as the desired lens design is directly included in the holographic calculation process with arbitrary degree of precision.

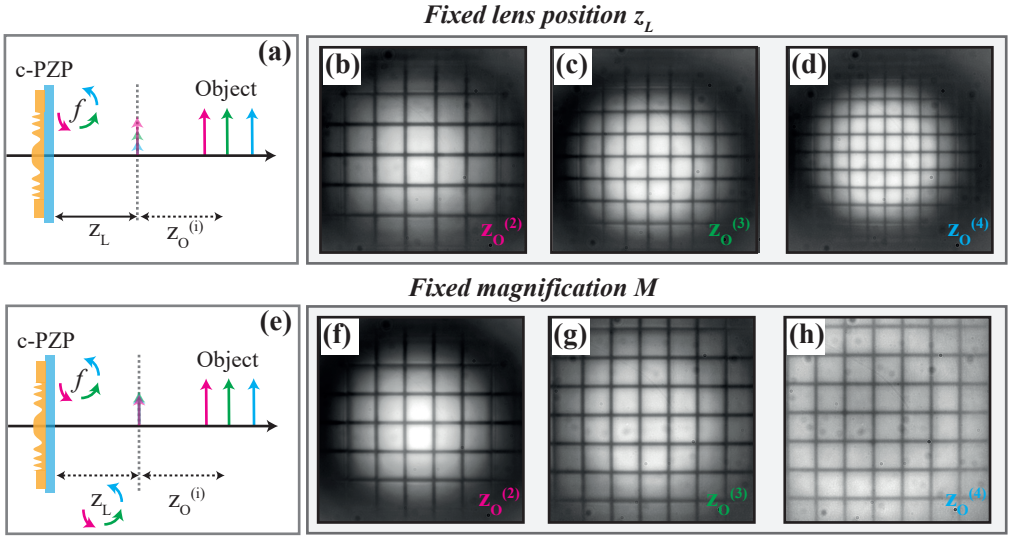

Fig. 6. Barlow lens configuration with fixed diffractive lens position and fixed magnification. (a) Representation of the working principle of a c-PZP Barlow lens with fixed position allowing object imaging through its focal length remodulation. (b-d) Optical images of the grid obtained for $z_O^{(i)}$ and $z_L^{(i)}$=−0.300 mm with c-PZP with focal length equal to $f^{(1)}$ = 0.4800 mm, $f^{(2)}$ = 0.4125 mm and $f^{(3)}$ = 0.3818 mm respectively. (e) Representation of the working principle of a c-PZP Barlow lens with tunable position and reshapable focal length allowing object imaging with controlled magnification. (f-h) Optical images of the grid obtained for $z_O^{(i)}$ with c-PZP with focal length equal to $f^{(1)}$ = 0.4142 mm, $f^{(2)}$ = 0.6627 mm and $f^{(3)}$ = 0.9112 mm placed at $z_L^{(1)}$=−0.270 mm, $z_L^{(2)}$=−0.430 mm and $z_L^{(3)}$=−0.590 mm respectively.

The c-PZP reconfiguration is achieved by erasing and reinscribing the azopolymer surface with a properly designed new surface relief geometry for the lens by irradiating the same area of the film with a new properly designed holographic pattern. It is worth mentioning that the reconfiguration of the azopolymer surface in our experimental configuration still requires the

Optics EXPRESS

movement of the azopolymer film in the lithographic plane ($z = 0$), where the writing holographic pattern is projected. Additionally, as the object to be imaged is placed close to the azopolymer surface, the erasure, in each reconfiguration step, is accomplished by irradiating the azopolymer film through the object itself, that has to be transparent. Both these limits could be in principle overcome by using a three-dimensional control over the holographic light pattern for structuring the surface in planes different from $z = 0$ [81] and by collimating the erasing beam through the same writing objective. With these clarifications, the results of Fig. 6(a-d) can be intended as a proof of concept of motionless multi-depth imaging system based on a varifocal diffractive lens.

As additional advanced configuration for the operation of the varifocal azopolymer c-PZP, we demonstrate in Fig. 6(e-h) a Barlow configuration able to maintain a fixed magnification in imaging objects at different positions of the optical axis. This requires the variation of both the position z_L and the focal length f of the Barlow lens (Fig. 6(e)) to simultaneously satisfy Eq. (9) and Eq. (10) for a fixed value M of the magnification. In the experiment of Fig. 6(f-h), a magnification $M = -0.35$ was fixed and the corresponding ratio z_L/f was calculated from Eq. (10). Then, the solutions $(z_L^{(i)}, f^{(i)})$ from Eq. (9) for different $z_O^{(i)}$ and fixed z_L/f have been used to define both the position and the focal length of the azopolymer c-PZP Barlow lens. As usual, the c-PZP focal length variation is achieved as holographically repeated erasing and rewriting steps of the azopolymer film surface. The direct measure of the magnification in the re-gained in-focus images of the object reported in Fig. 6(f-h), provided a value of M equal to -0.35 ± 0.02, -0.37 ± 0.02 and -0.36 ± 0.02, respectively, with the uncertainty dictated only by the positioning error of both the c-PZP and the object, and in perfect agreement with a constant magnification of the design.

In addition, as evidenced in the images Fig. 6(f-h), one should note that the imaging configuration with simultaneous translating/varifocal c-PZP results also in an effective reduction of the vignetting effect in a fixed region of interest of the image. This effect arises from the fact that the overall distance between the object and the diffractive lens increases passing from Fig. 6(f) to Fig. 6(h), with a larger number of light rays from the object that satisfy the condition of paraxial incidence. These results clearly demonstrate the advanced applications achievable with a hybrid microscope imaging system based on tunable varifocal diffractive lenses.

6. Conclusions

In this work we showed the realization of reshapable cosinusoidal phase zone plates through surface structuring of an azopolymer thin film. These phase-modulating diffractive lenses can be accurately designed using scalar diffraction theory and directly realized, in a single lithographic step, by exposing the surface of the azopolymer film to a computer-generated holographic intensity pattern. Precise focal length design and controlled diffraction efficiency are easily achievable through our lithographic method. The multifocal nature of the realized lenses, predicted by diffraction theory and characterized in our experiment, has been used to design an hybrid microscope imaging systems, capable to provide images of objects placed at any position of the optical axis. In addition, the all-optical reconfiguration of azopolymer films have been used here to realize varifocal diffractive lenses, that further extend the functionality of the hybrid microscope system. Tuning the focal length and the position of the diffractive lens provides simultaneous and independent control over the magnification, the field of view and the working distance of the hybrid imaging system, surpassing some of the limits of standard configurations based on Barlow lenses

As azopolymers can be optically erased, we demonstrated an in-place surface reshaping resulting in varifocal flat diffractive lenses. We also investigated focusing properties of these devices using a probe beam integrated in the holographic setup, demonstrating that the reshaping process preserves their efficiency and their overall quality: image formation from a phase diffractive lens obeys to a generalized conjugate planes equation, verified through experimental

Optics EXPRESS

results, allowing an easy design of optical systems based both on refractive and diffractive optics, also adding further useful degrees of freedom. As proof we have shown the possibility of using flat reshapable cosinusoidal phase zone plates to obtain a hybrid microscope capable of reconstructing in-focus images of small objects placed at different positions of the optical axis.

Our approach proves the advantages of flat shapeshifting optics as the basis of next-generation optical systems.

Funding. H2020 European Research Council (817794, research and innovation program "METAmorphoses"); Ministero dell'Istruzione, dell'Università e della Ricerca (CIR01_00015); Fondazione Cariplo (2019-3923).

Disclosures. The authors declare no conflicts of interest.

Data availability. Data underlying the results presented in this paper are not publicly available at this time but may be obtained from the authors upon reasonable request.

References

1. M. Born and E. Wolf, *Principles of Optics: Electromagnetic Theory of Propagation, Interference and Diffraction of Light*, 7th ed. (Cambridge University Press, 1999).
2. B. Saleh and M. Teich, *Fundamentals of Photonics*, 2nd Edition (Wiley-Interscience, 2007).
3. W. T. Chen and F. Capasso, "Will flat optics appear in everyday life anytime soon?" Appl. Phys. Lett. **118**(10), 100503 (2021).
4. P. Genevet, F. Capasso, F. Aieta, M. Khorasaninejad, and R. Devlin, "Recent advances in planar optics: from plasmonic to dielectric metasurfaces," Optica **4**(1), 139–152 (2017).
5. F. Capasso, "The future and promise of flat optics: a personal perspective," Nanophotonics **7**(6), 953–957 (2018).
6. W. Liu, H. Cheng, J. Tian, and S. Chen, "Diffractive metalens: from fundamentals, practical applications to current trends," Advances in Physics: X **5**(1), 1742584 (2020).
7. D. C. O'Shea, T. J. Suleski, A. D. Kathman, and D. W. Prather, *Diffractive Optics: Design, Fabrication, and Test* (SPIE Press, 2004).
8. B. C. Kress and P. Meyrueis, *Applied Digital Optics: From Micro-Optics to Nanophotonics* (Wiley, 2009).
9. A. Vijayakumar and S. Bhattacharya, *Design and Fabrication of Diffractive Optical Elements with MATLAB* (SPIE, 2017).
10. S. Sinzinger and M. Testorf, "Transition between diffractive and refractive micro-optical components," Appl. Opt. **34**(26), 5970–5976 (1995).
11. F. Aieta, M. A. Kats, P. Genevet, and F. Capasso, "Multiwavelength achromatic metasurfaces by dispersive phase compensation," Science **347**(6228), 1342–1345 (2015).
12. G. Andersen and D. Tullson, "Broadband antihole photon sieve telescope," Appl. Opt. **46**(18), 3706–3708 (2007).
13. X. Luo, "Subwavelength Artificial Structures: Opening a New Era for Engineering Optics," Adv. Mater. **31**(4), 1804680 (2019).
14. Q. Guo, Z. Shi, Y.-W. Huang, E. Alexander, C.-W. Qiu, F. Capasso, and T. Zickler, "Compact single-shot metalens depth sensors inspired by eyes of jumping spiders," Proc. Natl. Acad. Sci. **116**(46), 22959–22965 (2019).
15. S. Colburn and A. Majumdar, "Metasurface Generation of Paired Accelerating and Rotating Optical Beams for Passive Ranging and Scene Reconstruction," ACS Photonics **7**(6), 1529–1536 (2020).
16. A. Flores, M. R. Wang, and J. J. Yang, ""Achromatic hybrid refractive-diffractive lens with extended depth of focus," Appl. Opt. **43**(30), 5618–5630 (2004).
17. O. Cakmakci and J. Rolland, "Head-Worn Displays: A Review," J. Display Technol. **2**(3), 199–216 (2006).
18. G. Zhou, H. M. Leung, H. Yu, A. S. Kumar, and F. S. Chau, "Liquid tunable diffractive/refractive hybrid lens," Opt. Lett. **34**(18), 2793–2795 (2009).
19. G. Fluder, "Design of a hybrid refractive-diffractive telescope for observations in UV," Exp Astron **50**(2-3), 159–168 (2020).
20. E. T. F. Rogers, J. Lindberg, T. Roy, S. Savo, J. E. Chad, M. R. Dennis, and N. I. Zheludev, "A super-oscillatory lens optical microscope for subwavelength imaging," Nat. Mater. **11**(5), 432–435 (2012).
21. A. Yu, G. Chen, Z. Zhang, Z. Wen, L. Dai, K. Zhang, S. Jiang, Z. Wu, Y. Li, C. Wang, and X. Luo, "Creation of Sub-diffraction Longitudinally Polarized Spot by Focusing Radially Polarized Light with Binary Phase Lens," Sci Rep **6**(1), 38859 (2016).
22. O. Avayu, E. Almeida, Y. Prior, and T. Ellenbogen, "Composite functional metasurfaces for multispectral achromatic optics," Nat. Commun. **8**(1), 14992 (2017).
23. N. Mohammad, M. Meem, B. Shen, P. Wang, and R. Menon, "Broadband imaging with one planar diffractive lens," Sci Rep **8**(1), 2799 (2018).
24. M. M. Greve, A. M. Vial, J. J. Stamnes, and B. Holst, ""The Beynon Gabor zone plate: a new tool for de Broglie matter waves and hard X-rays? An off axis and focus intensity investigation," Opt. Express **21**(23), 28483–28495 (2013).
25. I. Mohacsi, I. Vartiainen, B. Rösner, M. Guizar-Sicairos, V. A. Guzenko, I. McNulty, R. Winarski, M. V. Holt, and C. David, "Interlaced zone plate optics for hard X-ray imaging in the 10 nm range," Sci Rep **7**(1), 43624 (2017).

Optics EXPRESS

26. M. Khorasaninejad, W. T. Chen, R. C. Devlin, J. Oh, A. Y. Zhu, and F. Capasso, "Metalenses at visible wavelengths: Diffraction-limited focusing and subwavelength resolution imaging," Science **352**(6290), 1190–1194 (2016).
27. H. Liang, Q. Lin, X. Xie, Q. Sun, Y. Wang, L. Zhou, L. Liu, X. Yu, J. Zhou, T. F. Krauss, and J. Li, "Ultrahigh Numerical Aperture Metalens at Visible Wavelengths," Nano Lett. **18**(7), 4460–4466 (2018).
28. W. T. Chen, A. Y. Zhu, J. Sisler, Z. Bharwani, and F. Capasso, "A broadband achromatic polarization-insensitive metalens consisting of anisotropic nanostructures," Nat. Commun. **10**(1), 355 (2019).
29. N. A. Rubin, G. D'Aversa, P. Chevalier, Z. Shi, W. T. Chen, and F. Capasso, "Matrix Fourier optics enables a compact full-Stokes polarization camera," Science **365**(6448), eaax1839 (2019).
30. V. Moreno, J. F. Román, and J. R. Salgueiro, "High efficiency diffractive lenses: Deduction of kinoform profile," Am. J. Phys. **65**(6), 556–562 (1997).
31. M. B. Fleming and M. C. Hutley, ""Blazed diffractive optics," Appl. Opt. **36**(20), 4635–4643 (1997).
32. K. Huang, F. Qin, H. Liu, H. Ye, C.-W. Qiu, M. Hong, B. Luk'yanchuk, and J. Teng, "Planar Diffractive Lenses: Fundamentals, Functionalities, and Applications," Adv. Mater. **30**(26), 1704556 (2018).
33. N. Lassaline, R. Brechbühler, S. J. W. Vonk, K. Ridderbeek, M. Spieser, S. Bisig, B. le Feber, F. T. Rabouw, and D. J. Norris, "Optical Fourier surfaces," Nature **582**(7813), 506–510 (2020).
34. M. Meem, A. Majumder, S. Banerji, J. C. Garcia, O. B. Kigner, P. W. C. Hon, B. Sensale-Rodriguez, R. Menon, and R. Menon, ""Imaging from the visible to the longwave infrared wavelengths via an inverse-designed flat lens," Opt. Express **29**(13), 20715–20723 (2021).
35. M. Meem, S. Banerji, C. Pies, T. Oberbiermann, A. Majumder, B. Sensale-Rodriguez, and R. Menon, ""Large-area, high-numerical-aperture multi-level diffractive lens via inverse design," Optica," Optica **7**(3), 252–253 (2020).
36. S. Banerji, M. Meem, A. Majumder, F. G. Vasquez, B. Sensale-Rodriguez, and R. Menon, ""Imaging with flat optics: metalenses or diffractive lenses?," Optica," Optica **6**(6), 805–810 (2019).
37. J. Engelberg and U. Levy, "The advantages of metalenses over diffractive lenses," Nat. Commun. **11**(1), 1991 (2020).
38. S. Nagelberg, L. D. Zarzar, N. Nicolas, K. Subramanian, J. A. Kalow, V. Sresht, D. Blankschtein, G. Barbastathis, M. Kreysing, T. M. Swager, and M. Kolle, "Reconfigurable and responsive droplet-based compound micro-lenses," Nat. Commun. **8**(1), 14673 (2017).
39. A. She, S. Zhang, S. Shian, D. R. Clarke, and F. Capasso, "Adaptive metalenses with simultaneous electrical control of focal length, astigmatism, and shift," Sci. Adv. **4**(2), 9957 (2018).
40. E. Arbabi, A. Arbabi, S. M. Kamali, Y. Horie, M. Faraji-Dana, and A. Faraon, "MEMS-tunable dielectric metasurface lens," Nat. Commun. **9**(1), 812 (2018).
41. A. M. Shaltout, V. M. Shalaev, and M. L. Brongersma, "Spatiotemporal light control with active metasurfaces," Science **364**(6441), eaat3100 (2019).
42. Y. Guo, M. Pu, X. Ma, X. Li, R. Shi, and X. Luo, "Experimental demonstration of a continuous varifocal metalens with large zoom range and high imaging resolution," Appl. Phys. Lett. **115**(16), 163103 (2019).
43. S. Colburn, A. Zhan, and A. Majumdar, ""Varifocal zoom imaging with large area focal length adjustable metalenses," Optica **5**(7), 825–831 (2018).
44. S. Colburn and A. Majumdar, "Simultaneous Achromatic and Varifocal Imaging with Quartic Metasurfaces in the Visible," ACS Photonics **7**(1), 120–127 (2020).
45. S. Wei, G. Cao, H. Lin, X. Yuan, M. Somekh, and B. Jia, "A Varifocal Graphene Metalens for Broadband Zoom Imaging Covering the Entire Visible Region," ACS Nano **15**(3), 4769–4776 (2021).
46. M. Y. Shalaginov, S. An, Y. Zhang, F. Yang, P. Su, V. Liberman, J. B. Chou, C. M. Roberts, M. Kang, C. Rios, Q. Du, C. Fowler, A. Agarwal, K. A. Richardson, C. Rivero-Baleine, H. Zhang, J. Hu, and T. Gu, "Reconfigurable all-dielectric metalens with diffraction-limited performance," Nat. Commun. **12**(1), 1225 (2021).
47. H.-S. Ee and R. Agarwal, "Tunable Metasurface and Flat Optical Zoom Lens on a Stretchable Substrate," Nano Lett. **16**(4), 2818–2823 (2016).
48. T. Zhan, K. Yin, J. Xiong, Z. He, and S.-T. Wu, "Augmented Reality and Virtual Reality Displays: Perspectives and Challenges," iScience **23**(8), 101397 (2020).
49. Z. Li, P. Lin, Y.-W. Huang, J.-S. Park, W. T. Chen, Z. Shi, C.-W. Qiu, J.-X. Cheng, and F. Capasso, "Meta-optics achieves RGB-achromatic focusing for virtual reality," Sci. Adv. **7**(5), eabe4458 (2021).
50. Y.-H. Lin, Y.-J. Wang, and V. Reshetnyak, "Liquid crystal lenses with tunable focal length," Liq. Cryst. Rev. **5**(2), 111–143 (2017).
51. S. L. Oscurato, F. Reda, M. Salvatore, F. Borbone, P. Maddalena, and A. Ambrosio, "Shapeshifting Diffractive Optical Devices," *Laser Photonics Rev.*, 2100514 (2022), early access.
52. S. L. Oscurato, F. Reda, M. Salvatore, F. Borbone, P. Maddalena, and A. Ambrosio, "Large-Scale Multiplexed Azopolymer Gratings with Engineered Diffraction Behavior," Adv. Mater. Interfaces **2101375**, 1–9 (2021).
53. D. Gabor, "A New Microscopic Principle," Nature **161**(4098), 777–778 (1948).
54. M. H. Horman and H. H. M. Chau, ""Zone Plate Theory Based on Holography," Appl. Opt. **6**(2), 317–322 (1967).
55. G. L. Rogers, "Gabor Diffraction Microscopy: the Hologram as a Generalized Zone-Plate," Nature **166**(4214), 237 (1950).
56. Z. Wang, S. Wang, P. Yang, and B. Xu, "Radial Shearing Interferometer Based on a Cosinusoidal Zone Plate," IEEE Photonics Technol. Lett. **31**, 1116–1119 (2019).
57. G. N. Watson, *A Treatise on the Theory of Bessel Functions*, 2nd ed. (Cambridge U.P., 1966).

Optics EXPRESS

58. S. L. Oscurato, M. Salvatore, P. Maddalena, and A. Ambrosio, "From nanoscopic to macroscopic photo-driven motion in azobenzene-containing materials," Nanophotonics **7**(8), 1387–1422 (2018).
59. F. Borbone, S. Luigi Oscurato, S. D. Sorbo, F. Pota, M. Salvatore, F. Reda, P. Maddalena, R. Centore, and A. Ambrosio, "Enhanced photoinduced mass migration in supramolecular azopolymers by H-bond driven positional constraint," J. Mater. Chem. C **9**(34), 11368–11375 (2021).
60. J. M. Ilnytskyi, V. Toshchevikov, and M. Saphiannikova, "Modeling of the photo-induced stress in azobenzene polymers by combining theory and computer simulations," Soft Matter **15**(48), 9894–9908 (2019).
61. K. Kim, H. Park, K. J. Park, S. H. Park, H. H. Kim, and S. Lee, "Light-Directed Soft Mass Migration for Micro/Nanophotonics," Adv. Opt. Mater. **7**(16), 1900074 (2019).
62. B. Yadav, J. Domurath, K. Kim, S. Lee, and M. Saphiannikova, "Orientation Approach to Directional Photodeformations in Glassy Side-Chain Azopolymers," J. Phys. Chem. B **123**(15), 3337–3347 (2019).
63. A. Priimagi and A. Shevchenko, "Azopolymer-based micro- and nanopatterning for photonic applications," Journal of Polymer Science Part B: Polymer Physics **52**(3), 163–182 (2014).
64. S. L. Oscurato, M. Salvatore, F. Borbone, P. Maddalena, and A. Ambrosio, "Computer-generated holograms for complex surface reliefs on azopolymer films," Sci. Rep. **9**(1), 6775 (2019).
65. A. Ambrosio, L. Marrucci, F. Borbone, A. Roviello, and P. Maddalena, "Light-induced spiral mass transport in azo-polymer films under vortex-beam illumination," Nat. Commun. **3**(1), 1–9 (2012).
66. H. Rekola, A. Berdin, C. Fedele, M. Virkki, and A. Priimagi, "Digital holographic microscopy for real-time observation of surface-relief grating formation on azobenzene-containing films," Sci Rep **10**(1), 19642 (2020).
67. J. Jelken and S. Santer, "Light induced reversible structuring of photosensitive polymer films," RSC Adv. **9**(35), 20295–20305 (2019).
68. M. Salvatore, F. Borbone, and S. L. Oscurato, "Deterministic Realization of Quasicrystal Surface Relief Gratings on Thin Azopolymer Films," Adv. Mater. Interfaces **7**(11), 1902118 (2020).
69. Y. Lim, B. Kang, S. J. Hong, H. Son, E. Im, J. Bang, and S. Lee, "A Field Guide to Azopolymeric Optical Fourier Surfaces and Augmented Reality," Adv. Funct. Mater. **31**(39), 2104105 (2021).
70. M. Pasienski and B. DeMarco, ""A high-accuracy algorithm for designing arbitrary holographic atom traps," Opt. Express **16**(3), 2176–2190 (2008).
71. J. W. Goodman, ""Some fundamental properties of speckle," J. Opt. Soc. Am. **66**(11), 1145–1150 (1976).
72. J. Vapaavuori, R. H. A. Ras, M. Kaivola, C. G. Bazuin, and A. Priimagi, "From partial to complete optical erasure of azobenzene–polymer gratings: effect of molecular weight," J. Mater. Chem. C **3**(42), 11011–11016 (2015).
73. J. W. Goodman, *Introduction to Fourier Optics* (Roberts and Company Publishers, 2005).
74. D. Voelz, *Computational Fourier Optics: A MATLAB Tutorial* (Society of Photo Optical, 2011).
75. B. D. Guenther and D. Steel eds., *Encyclopedia of Modern Optics*, 2nd edition (Academic Press, 2018).
76. E. Hecht, *Optics*, 4th edition (Addison-Wesley, 2001).
77. M. Khorasaninejad, W. T. Chen, A. Y. Zhu, J. Oh, R. C. Devlin, C. Roques-Carmes, I. Mishra, and F. Capasso, "Visible Wavelength Planar Metalenses Based on Titanium Dioxide," IEEE J. Sel. Top. Quantum Electron. **23**(3), 43–58 (2017).
78. S. J. Anderson, "The Barlow lens," J. Brit. Astro. Assoc. **92**(3), 135–136 (1982).
79. S. Banerji, M. Meem, A. Majumder, B. Sensale-Rodriguez, and R. Menon, "Imaging over an unlimited bandwidth with a single diffractive surface," arXiv:1907.06251 [physics] (2019).
80. S. Banerji, M. Meem, A. Majumder, J. C. Garcia, P. Hon, C. Pies, T. Oberbiermann, B. S. Rodriguez, R. Menon, and R. Menon, "Inverse Designed Flat Optics with Diffractive Lenses," in *Imaging and Applied Optics Congress (2020), Paper ITh5E.3* (Optical Society of America, 2020), p. ITh5E.3.
81. J. Leach, K. Wulff, G. Sinclair, P. Jordan, J. Courtial, L. Thomson, G. Gibson, K. Karunwi, J. Cooper, Z. J. Laczik, and M. Padgett, ""Interactive approach to optical tweezers control," Appl. Opt. **45**(5), 897–903 (2006).